


# Cathodoluminescence in single and multiwall $WS_2$ nanotubes: Evidence for quantum confinement and strain effect


Cite as: Appl. Phys. Rev. **7**, 041401 (2020); <https://doi.org/10.1063/5.0019913>

Submitted: 26 June 2020 . Accepted: 22 September 2020 . Published Online: 21 October 2020

S. Ghosh , V. Brüser , I. Kaplan-Ashiri , R. Popovitz-Biro, S. Peglow , J. I. Martínez , J. A. Alonso , and A. Zak 

## COLLECTIONS

 This paper was selected as Featured

 This paper was selected as Scilight



View Online



Export Citation



CrossMark

## ARTICLES YOU MAY BE INTERESTED IN

[Tungsten disulfide nanotubes demonstrate useful luminescent behavior](#)

Scilight **2020**, 431103 (2020); <https://doi.org/10.1063/10.0002409>

[Application of ion beam technology in \(photo\)electrocatalytic materials for renewable energy](#)

Applied Physics Reviews **7**, 041303 (2020); <https://doi.org/10.1063/5.0021322>

[Elastocaloric switching effect induced by reentrant martensitic transformation](#)

Applied Physics Reviews **7**, 031406 (2020); <https://doi.org/10.1063/5.0007753>

AVS Quantum Science

SUBMIT TODAY!



SPECIAL ISSUE: Optical Micro-manipulation of Quantum Systems

Co-Published by



# Cathodoluminescence in single and multiwall WS<sub>2</sub> nanotubes: Evidence for quantum confinement and strain effect



Cite as: Appl. Phys. Rev. **7**, 041401 (2020); doi: 10.1063/5.0019913

Submitted: 26 June 2020 · Accepted: 22 September 2020 ·

Published Online: 21 October 2020



S. Ghosh,<sup>1</sup> V. Brüser,<sup>2</sup> I. Kaplan-Ashiri,<sup>3</sup> R. Popovitz-Biro,<sup>3</sup> S. Peglow,<sup>4</sup> J. I. Martínez,<sup>5</sup> J. A. Alonso,<sup>6</sup> and A. Zak<sup>1,a)</sup>

## AFFILIATIONS

<sup>1</sup>Faculty of Sciences, Department of Physics, Holon Institute of Technology, Holon 5810201, Israel

<sup>2</sup>Department of Plasma Process Technology, Leibnitz Institute for Plasma Science and Technology, Greifswald 17489, Germany

<sup>3</sup>Department of Chemical Research Support, Weizmann Institute of Science, Rehovot 76100, Israel

<sup>4</sup>Department of Environmental Physics, Institute of Physics, University of Greifswald, Greifswald 17489, Germany

<sup>5</sup>Department of Nanostructures and Low-dimensional Materials, Institute of Materials Science of Madrid, Madrid 28049, Spain

<sup>6</sup>Department of Theoretical, Atomic and Optical Physics, University of Valladolid, 47011 Valladolid, Spain

<sup>a)</sup>Author to whom correspondence should be addressed: [alzak@hit.ac.il](mailto:alzak@hit.ac.il)

## ABSTRACT

For nanoparticles with sub-10 nm diameter, the electronic bandgap becomes size dependent due to quantum confinement; this, in turn, affects their electro-optical properties. Thereby, MoS<sub>2</sub> and WS<sub>2</sub> monolayers acquire luminescent capability, due to the confinement-induced indirect-to-direct bandgap transition. Rolling up of individual layers results in single wall inorganic nanotubes (SWINTs). Up to the present study, their luminescence properties were expected to be auspicious but were limited to theoretical investigations only, due to the scarcity of SWINTs and the difficulties in handling them. By optimizing the conditions in the plasma reactor, relatively high yields of WS<sub>2</sub> SWINTs 3–7 nm in diameter were obtained in this work, compared to previous reports. A correlative approach, transmission electron microscopy coupled with a scanning electron microscope, was adapted to overcome handling obstacles and for testing individual nanotubes by low-temperature cathodoluminescence. Clear cathodoluminescence spectra were obtained from WS<sub>2</sub>-SWINTs and compared with those of WS<sub>2</sub> multiwall nanotubes and the corresponding bulk material. Uniquely, the optical properties of INTs acquired from cathodoluminescence were governed by the opposite impact from quantum size effect and strain in the bent triple S-W-S layers. The experimental findings were confirmed by the Density Functional and Time-Dependent Density Functional theoretical modeling of monolayer and bilayer nanotubes of different chiralities and diameters. This study provides experimental evidence of the quantum confinement effect in WS<sub>2</sub> SWINTs akin to WS<sub>2</sub> monolayer. The ability to tune the electronic structure with morphology or number of layers may be exploited toward photoelectrochemical water splitting with WS<sub>2</sub> catalysts, devising field effect transistors, photodetectors, and so on.

© 2020 Author(s). All article content, except where otherwise noted, is licensed under a Creative Commons Attribution (CC BY) license (<http://creativecommons.org/licenses/by/4.0/>). <https://doi.org/10.1063/5.0019913>

## I. INTRODUCTION

Electronic properties of layered transition metal dichalcogenide (TMD) nanostructures are closely related to their morphology (planar, spherical, or tubular), as well as to their size, number of layers, and chirality (for nanotubes). A classic example validating this phenomenon is the confinement-induced indirect-to-direct bandgap transition observed in molybdenum disulphide (MoS<sub>2</sub>)<sup>1,2</sup> and tungsten disulfide (WS<sub>2</sub>)<sup>3,4</sup> by exfoliating bulk 2H-MoS<sub>2</sub>/2H-WS<sub>2</sub> to a monolayer. The energy gap of the indirect transition progressively

increases as the number of layers decreases, which is attributed to quantum size effect, and becomes so high in a monolayer that the material converts into a direct bandgap semiconductor. Consequently, a dramatic enhancement of the luminescence quantum efficiency by a factor of more than 10<sup>4</sup> was observed in MoS<sub>2</sub> monolayers<sup>1</sup> compared to their bulk counterparts. Similarly, an increase in photoluminescence quantum yield by factors ~10 and ~10<sup>3</sup> was recorded from a WS<sub>2</sub> bilayer and monolayer,<sup>4</sup> respectively, compared to the bulk material.

The direct bandgap offers a plethora of optoelectronic applications for these TMD monolayers, including those in switchable electronics. Field effect transistors fabricated of MoS<sub>2</sub> and WS<sub>2</sub> monolayers demonstrated a room-temperature high carrier mobility and exceptionally large current ON-OFF ratio.<sup>5,6</sup> Logical circuits and amplifiers prepared of these 2D systems were also tested.<sup>7,8</sup> In addition, emerging from their band structures, atomic monolayers of both MoS<sub>2</sub> and WS<sub>2</sub> exhibit strong excitonic effects, extremely high optical responsivity, a near-unity quantum yield luminescence,<sup>9,10</sup> and efficient valley polarization for spintronics.<sup>11,12</sup>

The dependence of the bandgap on the number of layers in zero-dimensional (0D) WS<sub>2</sub> inorganic fullerene-like (IF) nanoparticles (NPs) was investigated by Frey *et al.*<sup>13</sup> In these NPs the layers are bent into co-spheres creating onion-like configurations, but retain the structure inherent to bulk 2H-WS<sub>2</sub>: van der Waals bonding between the 2H-stacked layers and trigonal prismatic arrangement of the covalently bonded S and W atoms inside the layer. The IF NPs were obtained by sulfurization of tungsten oxide NPs in the outside-inward mechanism described by Feldman *et al.*<sup>14</sup> The growth features in the initial stages of the synthesis of these NPs lead to the formation of the first few WS<sub>2</sub> layers conformably to the surface of the encapsulated tungsten suboxide core. For IF-WS<sub>2</sub>, 15–350 nm in diameter with a few ( $n < 5$ ) WS<sub>2</sub> external layers, a blue shift of the A and B excitonic energies in the absorption spectra was recorded as compared to bulk 2H-WS<sub>2</sub>. This blue shift was ascribed to the carrier confinement in a direction parallel to the *c*-axis (or *z* direction, perpendicular to the layers) similar to the quantum size effect observed in atomically thin sheets of MoS<sub>2</sub> and WS<sub>2</sub>.<sup>1–4</sup> Unexpectedly, IF-WS<sub>2</sub> NPs with a number of layers from  $n = 6$  and beyond exhibited reduction of the A and B exciton energies compared to the bulk.<sup>13</sup> Moreover, the shrinkage of the gap became larger as additional inner layers (of smaller diameters) were formed along with the reaction (sulfurization) time at the expense of the oxide core. This red shift, intrinsic to layered nanostructures, was ascribed to the deformations, curvature, and discommensuration between adjacent atomic layers that the structure must accommodate in order to form multilayered IF NPs.<sup>13,15</sup>

Similar shrinkage of the gap for inorganic nanotubes (INTs, the layers of which are bent into coaxial cylinders) of different TMDs (GaS,<sup>16</sup> GaSe,<sup>17</sup> and MoS<sub>2</sub><sup>18</sup>) and sizes, compared to the bulk material, has been predicted theoretically, but confirmed experimentally for multiwall nanotubes of WS<sub>2</sub><sup>19,20</sup> and MoS<sub>2</sub>,<sup>21</sup> only. Measurements based on resonant Raman spectroscopy,<sup>19</sup> for example, show that the A-exciton transition energy (with  $\sim 50$  meV binding energy) of multilayered WS<sub>2</sub> nanotubes is lower than the bulk value (1.98 eV). Moreover, it becomes smaller (reducing from 1.95 to 1.91 eV) with decreasing nanotube diameter (in the range from 121 to 46 nm, respectively) implying a red shift, which is in contrast to what one would expect from the quantum confinement effect. These results were ascribed to enhanced strain, incorporated in the walls of TMDs' nanotubes with the reduction in size, and they confirmed the theoretical predictions of Seifert *et al.*<sup>22,23</sup> for smaller INTs (2–5 nm). It was shown<sup>22</sup> that the strain energy in the rolled triple X-M-X (X-chalcogenide, M-metal) layers follows roughly a  $1/D^2$  behaviour, with *D* being the tube diameter. The lowered *D* resulted in increased strain and in a subsequent gap size shrinkage (red shift).

Both IFs and INTs did not exhibit a carrier confinement parallel to the layers (in spite of their nano size), due to the relatively small

exciton radius in the *a-b* plane (*xy* direction) and the closed-shell (effectively infinite) structure.<sup>13,24</sup> All these works<sup>13–25</sup> demonstrated that the semiconductor character of WS<sub>2</sub> and MoS<sub>2</sub> materials is preserved in the IF and INT structures. The electronic structure of individual WS<sub>2</sub> multiwall nanotubes (MWINT) measured by electron energy loss spectra (EELS)<sup>25</sup> exhibited a small indirect bandgap ( $\sim 1.3$  eV) and a moderate direct bandgap ( $\sim 1.8$  eV), which is smaller than the bulk value of  $\sim 2.05$  eV.<sup>13</sup>

The bandgap of single wall MoS<sub>2</sub> and WS<sub>2</sub> nanotubes (SWINT) was investigated theoretically.<sup>22,26,27</sup> In general, nanotubes with two types of electronic structure depending on their chirality, were observed: armchair (*n, n*) nanotubes were found to exhibit a small indirect and moderate direct gap, while zigzag (*n, 0*) nanotubes possess a small direct gap. It was shown<sup>22,26</sup> that the size of the gaps depends upon diameter and chirality of the nanotube, always being smaller than the corresponding bulk value.

Thus, up until the current study experimental results reporting the bandgap profile in WS<sub>2</sub>/MoS<sub>2</sub> nanotubes focused on MWINTs,<sup>19,20,25</sup> while studies of SWINTs are limited to theoretical works<sup>22,26,27</sup> only. In this work we report the experimental CL spectra from SWINT nanotubes (3–7 nm in diameter) at low temperatures ( $-140$  °C) and compare them with those of multiwall tubes and exfoliated flakes.

Through this investigation, clear CL spectra have been observed for SWINTs. The obtained peak was assigned to the direct bandgap with the energy (1.98 eV) blue shifted compared to MWINTs (1.87 eV), whose value is compatible with previous EELS measurements.<sup>25</sup> Both SWINTs and MWINTs reveal red shift compared to the bulk WS<sub>2</sub> bandgap (2.01–2.07 eV),<sup>19,22,26,28,29</sup> which is in accordance with theoretical predictions<sup>22,26</sup> and some experimental results,<sup>19,20</sup> and similar to the IF-WS<sub>2</sub> behaviour.<sup>13</sup> The increase in bandgap energy in the SWINT compared to the MWINT was theoretically predicted earlier<sup>30</sup> but has not been realized experimentally so far.

The synthesis of single wall nanotubes from layered TMD compounds is not a trivial task. Smaller diameter with a consequent smaller radius of curvature for nanotubes renders them unstable owing to high strain energy. Calculations based on Density Functional Tight-Binding Theory (DFTB) show that the strain energy in their triple (X-M-X) layers is about an order of magnitude larger than that of carbon nanotubes with similar diameter.<sup>22,26</sup> This causes the complicity in the synthesis of such structures and points to the need of highly energetic conditions for their preparation. To achieve these conditions, high-energy plasma was used in this study to produce SW nanotubes of WS<sub>2</sub>. The details of this process were previously reported.<sup>31</sup> The current study brought new insights into the reaction protocol, resulting in reproducible production of WS<sub>2</sub> SWINTs in significant amounts, bestowing an opportunity for experimental study of their optical properties and determination of their bandgap energy that has been unavailable hitherto.

The experimental findings have been substantiated by modeling with Density Functional Theory (DFT) and Time-Dependent Density Functional Theory (TDDFT), where monolayer and bilayer nanotubes of different chiralities and diameters have been considered. The theoretical findings clearly show an increased bandgap for monolayer tubes compared to double-wall tubes, which is in agreement with the experimentally measured CL data. A blue shift of 0.22 to 0.45 eV was obtained by comparing the calculated photoabsorption spectra of single wall vs double wall WS<sub>2</sub> nanotubes for different external diameters. The largest calculated diameters are in close agreement with

experimentally observed SWINTs. The threshold energies of the single wall tubes were consistently larger than those of the double wall tubes.

The study is particularly important as it provides future opportunities for bandgap engineering<sup>32,33</sup> as a function of the number of layers and dimension of the nanotubes.

## II. EXPERIMENTAL

A recently developed synthetic protocol<sup>31</sup> could produce WS<sub>2</sub> 1–3 layered hollow nanotubes with 3–7 nm diameter and 20–100 nm length using WS<sub>2</sub> multiwall (MW) nanotubes as precursor.

Highly exergonic conditions, required for this synthesis, were realised through high-power, inductively coupled radio frequency plasma irradiation. Plasma treatment of multiwall nanotubes caused cutting of fragments from the MWINT external layers along specific crystallographic orientations or line defects. Subsequently, the monolayer or few layer flakes, depends on reaction conditions, exfoliated and furled in the opposite direction and seamed, resulting in generation of single wall (SW) to few layer WS<sub>2</sub> nanotubes. In addition to the strong interaction of the highly energetic plasma with the outer surface of the parent multiwall nanotubes, the formation of tubular structures is simultaneously governed by a release of the large elastic strain stored in the walls of MWINTs and by the presence of dangling bonds at the reactive edges of the fragments. The entire scheme representing the growth mechanism of single wall, “daughter,” INTs is depicted in Fig. 1.

The MW (parent) INTs of WS<sub>2</sub> were produced through reduction and evaporation of the tungsten oxide precursor, growth of suboxide 1D nanowhiskers, and their following sulfurization to tungsten sulphide nanotubes. A protocol for this reaction route was conceived<sup>34</sup> and optimized<sup>35</sup> for scalable synthesis of WS<sub>2</sub> nanotubes. As synthesized MWINTs went through a deagglomeration procedure involving ultrasonication (US) of the nanotubes in a US bath for 1 min using acetone, as the dispersing medium. Toward synthesis of SWINTs, the acetone suspension with MWINT precursor was deposited on a flexible tungsten substrate. A thin film of MWINTs was formed after evaporation of the acetone.

Subsequently, these MW nanotubes were subjected to pre-annealing at temperatures that varied from 350 °C to 500 °C in a vacuum over a time period, which was also varied from 15 to 40 min. Then, clean of organic residuals, the MWINT films were exposed to argon (Ar) plasma coupled with high temperature. The various process parameters, which were optimized, include argon pressure,

amount of parent MWINTs, pre-annealing temperature and time, plasma power, temperature at which the MWINT surface was exposed to the plasma, bias voltage, and plasma treatment duration. The argon pressure was studied in the range of 10 Pa to 1000 Pa. The power of the plasma irradiation was systematically varied between 150 to 650 W based on our previous experience of producing SWINT.<sup>31</sup> The MWINT samples were subjected to test conditions comprising a temperature varied from 350 °C to 600 °C in conjunction with simultaneous plasma irradiation applied for 1, 5, 20, or 40 minutes. The experimental setup, presented in Fig. S1 of the [supplementary material](#), was also modified to implement combined heating and negative bias voltage (from –40 to –70 V) in order to enhance the kinetic energy of the argon ions.

In addition, the effect on SWINTs’ yields through variation of the parent MWINTs’ layer thickness on the tungsten substrate was studied. Other efforts to optimize the yield of SWINTs involved using of a nickel mesh and application of a positive bias (+12 V) to attenuate the effect of plasma on the MW nanotubes.

The SW tubes thus produced were analysed by high-resolution transmission electron microscopy (HR-TEM) using a JEOL 2100 microscope operating at 200 kV and a scanning electron microscope (SEM), JSM 7500F JEOL. Grazing Incidence X-ray Diffraction (GIXRD) patterns of powders before and after plasma treatment, discussed in the [supplementary material](#), were obtained with a Bruker D8 Advance diffractometer with measurements performed at an incident angle  $\omega = 0.5^\circ$  over a range of 10°–80° for 2 $\Theta$  (2 Theta) with a step width of 0.02° and 5 s per step.

The CL studies were preformed using a Gatan MonoCL4 Elite detector and spectrometer, which is installed on a high-resolution scanning electron microscope (HRSEM), Zeiss Gemini SEM 500. The SEM is also equipped with a cryo-stage by Leica Microsystems. However, since the resolution of the SEM while acquiring CL is limited, the SWINTs cannot be observed. To overcome this challenge a correlative approach was adapted between the SEM-CL and the TEM. In particular, the samples were imaged with TEM, and the SWINTs were mapped on the grid so they can be located later in the SEM-CL.

For this purpose, marked TEM finder grids (Electron Microscopy Sciences, EMS grid, 400 mesh, Holey Carbon coated) were utilized to immobilize the SWINTs. Once the locations of the SWINTs on the grid were determined through TEM, these grids were

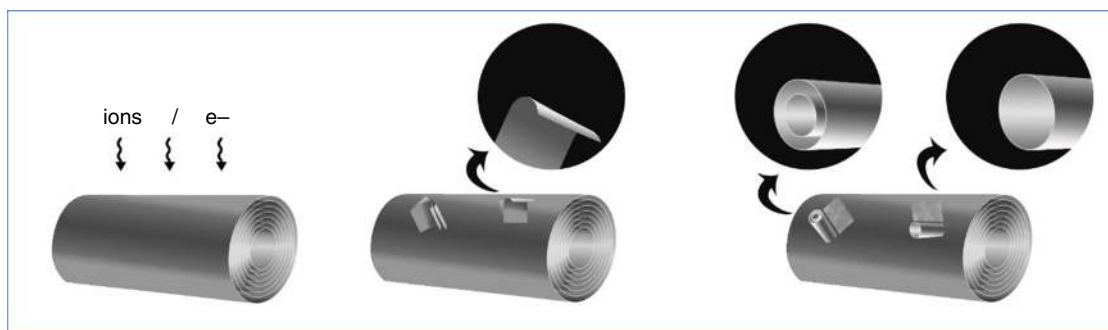


**FIG. 1.** Growth mechanism of “daughter” SWINTs showing plasma ions’ bombardment of MWINT, cutting and exfoliation of nanostripes with dangling bonds along their edges. The stripes furl to form single to few layer nanotubes, which is an energetically favourable structure.

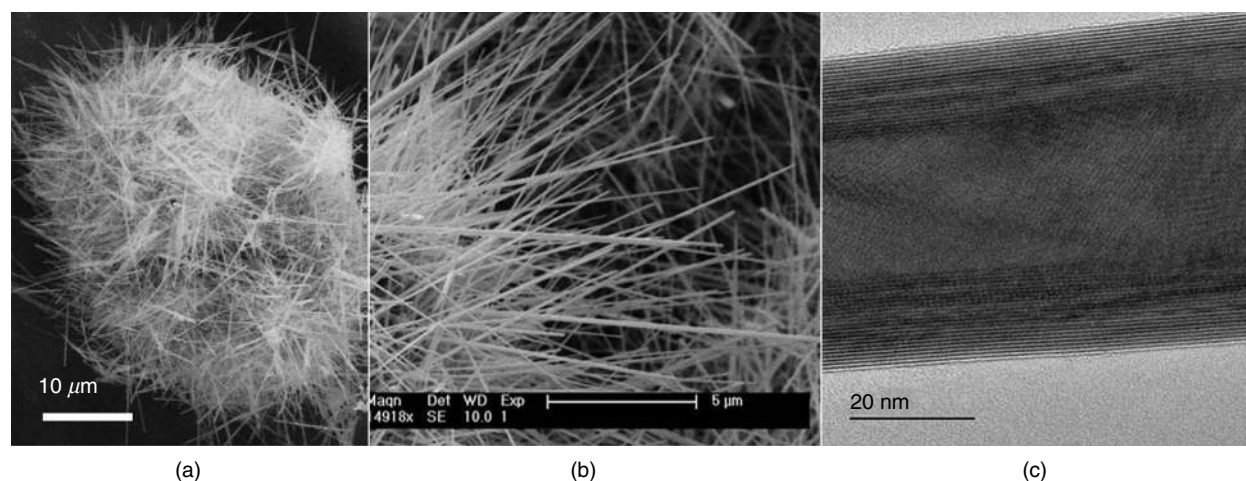


**FIG. 2.** (a, b) Scanning electron microscopy images at different magnifications showing phase purity of the multiwall  $\text{WS}_2$  nanotubes grown in the urchin-like agglomerates. (c) Transmission electron microscopy image of an individual multiwall nanotube 56 nm in diameter and consisting of 24 layers.

used as a sample for CL examination via HRSEM. Among all the solutions used, ethanol as a dispersing medium with a sonication period of 1 min, proved to be the best for sample preparation for TEM studies. X-ray photoelectron spectroscopy (XPS) was acquired by an Axis Ultra DLD Kratos instrument.

### III. RESULTS AND DISCUSSION

#### A. Synthesis and characterization of SWINTs

The synthesized MWINT of  $\text{WS}_2$  are obtained as urchin type agglomerates. Their scanning electron microscope analysis at two different magnifications and associated TEM image of an untreated precursor MW nanotube are presented in Figs. 2(a) through 2(c). The SEM images [Figs. 2(a) and 2(b)] confirm a pure nanotubes phase and the length of the nanotubes varied from 2 to 20  $\mu\text{m}$ . Figure 2(c) presents a TEM image showing a MWINT having 24 layers with a diameter of 56 nm.

As evident from the SEM images of a cluster of multiwall nanotubes, the agglomeration of synthesized tubes was detrimental toward

exposing the maximum surface area to plasma. Thus, the nanotubes were deagglomerated and dispersed before exposure to the plasma. A black thin film of such nanotubes on the tungsten substrate after evaporation of acetone exhibits flat surface and good dispersion as shown in Figs. 3(a) and 3(b), respectively.

At the preliminary stages of this study, the dispersion of MWINTs in organic solution reduced the yield of the SWINTs [Fig. 3(c)]. This understanding, eventually led to the introduction of a post deagglomeration pre-annealing step (prior to the plasma etching), which was necessary for removal of carbon traces and proper plasma-MWINTs' surface interaction. Subsequently, the MWINTs were plasma irradiated with simultaneous heating of the INTs to strengthen the exergonic conditions of the reaction. The heating was possibly very important also for promoting the seaming of the exfoliated  $\text{WS}_2$  monolayers and formation of the nanotubes. The heating of the MWINT was controlled via temperature of the tungsten substrate. Improved dispersion of the INTs on the tungsten substrate resulted in a better thermal contact of the INTs with the substrate.

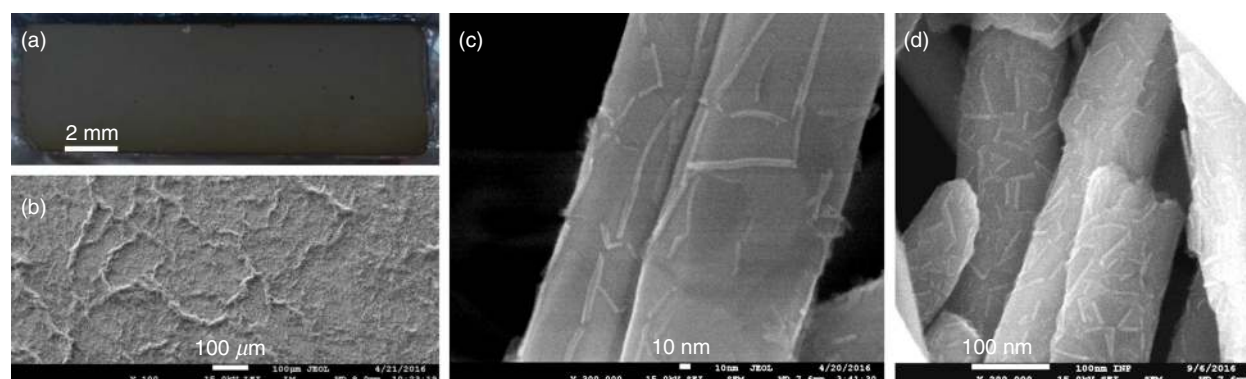


**FIG. 3.** (a) Photograph of  $\text{WS}_2$  MWINTs film precursor deposited on tungsten substrate ( $15 \times 45 \text{ mm}^2$ ) after dispersion in acetone. (b) Scanning electron microscopy high magnification image of the  $\text{WS}_2$  MWINTs film showing its carpet-like surface. (c) Small amount of SWINT after plasma treatment without pre-annealing. (d) Large amount of SWINT after addition of a pre-annealing step at 350  $^\circ\text{C}$ .

On the long way to the optimization, the influence of various parameters on SWINTs production yield was investigated. Among them: pre-annealing temperature and time, plasma power and Ar pressure, temperature at which the MWINT surface was exposed to the plasma, the plasma treatment time, and applied bias voltage. The optimization of these parameters resulted in the dual-step plasma-synthesis parameters: pre-annealing of the deagglomerated precursor at 350 °C for 40 min, and thereafter, treatment in Ar plasma of 10 Pa at a power of 600 W along with a thermal treatment at 500 °C, applied for 40 min. The optimized synthesis parameters for acquiring high yield of SWINTs through plasma exposure of MWINTs are collated in Table I of the [supplementary material](#). This procedure enhanced the formation of SW tubes and resulted in their high yield [see Fig. 3(d)]. The SEM images of plasma-treated samples for different combinations of plasma power, pre-annealing conditions, plasma exposure time, and temperature to achieve the desired structure and yield for the SWINTs from the MW precursor tubes are collated in Figs. S2(a) through S2(e) of the [supplementary material](#).

Along with tracking the production yield of the daughter (single wall) tubes, profiling the plasma-treated powder was imperative to avoid the formation of any unwanted by-product from the plasma treatment. This is particularly important as Ar plasma was reported to cause oxidative unzipping of carbon nanotubes (CNTs) and consequent formation of C = O complexes.<sup>36</sup> This prompted the XRD and XPS analyses of the samples containing a high concentration of SW nanotubes. The XRD pattern presented in Fig. S3 (see the [supplementary material](#)) attests to the phase integrity of the plasma treated samples. All the peaks originating from the sample containing SWINT are congruent with the peaks of the precursor WS<sub>2</sub> tubes implying that no new phase has been formed. Analysing the XPS spectra on Fig. 4 further corroborated the phase purity of the plasma treated samples.

The XPS survey revealed signals characteristic exclusively of tungsten and sulphur. The presence of carbon is attributed to the C 1s peak used as a reference for correcting peak shifts. Peaks at 162.5 and 163.6 eV can be associated with the sulphur 2p<sub>3/2</sub> and 2p<sub>1/2</sub> orbitals, respectively, while those at 33.1, 35.4, and 38.5 eV originate from the W 4f<sub>7/2</sub>, W 4f<sub>5/2</sub>, and W 5p<sub>3/2</sub> orbitals.<sup>37</sup> An apparent reduction in the absolute intensity of the peaks for the plasma treated samples is ascribed to the dilution of atoms at the surface from the imposed exergonic conditions.

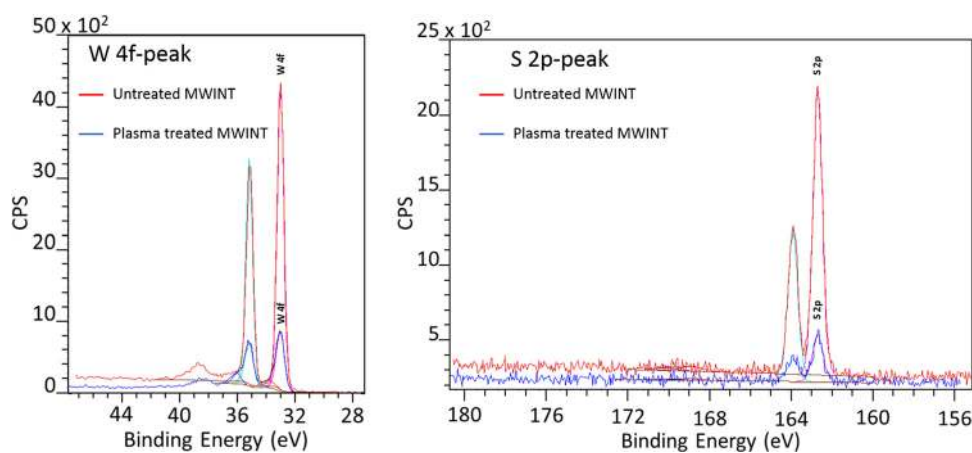


**FIG. 4.** XPS spectra of pristine and plasma treated WS<sub>2</sub> MWINTs showing peaks at similar binding energies. The reduction in intensity is ascribed to the dilution of atoms at the surface as a result of plasma interaction with INTs.

## B. TEM correlated cathodoluminescence (CL) measurements

The CL studies were performed through HRSEM. To overcome the low resolution of this microscope during CL measurements, the precise localization of the SWINT was done by means of HRTEM prior to CL study. The marked TEM finder grids were utilized to immobilize the SWINTs. Once the locations of the SWINTs on the marked grid were determined via TEM, these grids were used as a sample for the CL measurement on HRSEM.

### 1. Sample preparation

Since the phase integrity of the samples after the plasma treatment was established via XRD and XPS, the subsequent step of dispersing the powder in an organic medium toward CL study was undertaken. It was a nontrivial effort to separate the SWINTs from the MWINTs, given the small dimensions of these nanotubes and an ensuing van der Waals interaction with the MWINT together with the tendency of the nanostructures to form agglomerates. Different dispersing media either in its pristine form or laced with certain ionic or non-ionic surfactants were tested. In the present study, among all solvents, ethanol without any form of surfactants was found to be the best way for separating the SWINTs from the MWINTs. The SWINTs were removed from the surface of MWINTs, but remained entrapped in the flaky regions next to the MWINT. Thus, the dispersed solution was comprised of both single wall and multiwall nanotubes along with flaky regions. Sonication time also played a prominent role in dispersing the system as imparting energy through sustained sonication beyond a threshold period often damaged the small nanotubes irreparably. Dispersion stability of the nanotubes in a medium was highlighted through the intensity of the UV-visible absorption (extinction) spectrum. This technique was utilized previously towards sorting of WS<sub>2</sub> nanotubes with varying diameters.<sup>38</sup> The UV-visible spectroscopy, performed in the reflectance mode, exhibits the extinction spectrum (including absorption and scattering) shown in Fig. 5. The obtained peaks, originating at 684 nm, 575 nm, and a shoulder at ca. 504 nm, are of polaritonic nature and might be ascribed to strong coupling effect between optical cavity modes confined in the nanotubes and their two excitons.<sup>39,40</sup> The excitons of WS<sub>2</sub> are

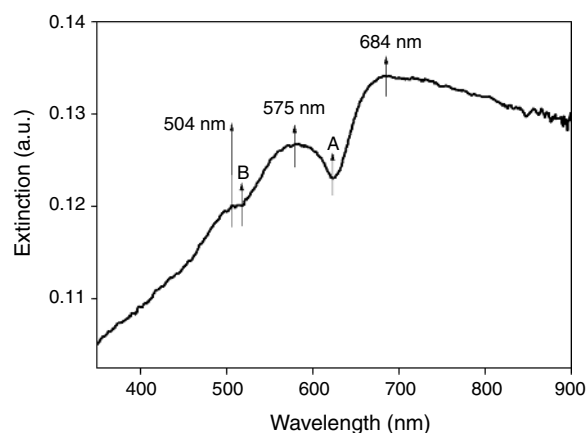


**FIG. 5.** UV-visible (extinction) spectrum of a plasma treated sample comprising both SW and MW nanotubes. The extinction spectrum acquired in reflectance mode highlights the A and B excitons at the dips, while the polaritonic branches are observed at 575 and 684 nm.

typically observed at 630 nm (A) and 520 nm (B), which are almost identical with the dips in the current extinction spectrum clearly visible at  $\sim 623$  and  $\sim 518$  nm.<sup>40</sup>

A strong absorbance (extinction) signal highlighted in the UV-visible spectrum implies a stable dispersion of the nanotubes. Thus, samples with the best spectra (or most stable dispersion) were finally chosen for HRTEM analysis, and subsequently, for CL measurements on HRSEM.

It should be noted that UV-visible spectroscopy is a potent tool to determine the crystallite size dependence of the bandgap by considering inter-band transitions of excitons. However, the UV-vis spectrum in our case was not feasible for determining the band profiles of SWINTs as it was impossible to fully segregate the SWINTs from the MWINTs and obtain a homogeneous solution containing exclusively the former. Contrarily, a focused electron beam at a high magnification of electron microscope during the CL studies was impinged for probing the bandgap transitions of SWINTs solely. Once the position of SWINT was fixed on the TEM grid, the grid was transferred to SEM to perform the CL analysis. Through this correlative technique, TEM coupled with SEM, a spatial resolution sub-10 nm<sup>41</sup> and of even 1 nm<sup>42</sup> could be achieved, which is much more feasible for extracting the bandgap information pertinent to the SWINTs.

## 2. TEM correlated CL measurements

Transmission electron microscopy images for the single layer structures are shown in Fig. 6. In addition to entrapped SW nanotubes in the exfoliated zones, scrolls and furls can be also observed in the vicinity of the multiwall tubes.

The TEM correlated CL studies provide the resolution necessary to identify and examine the regions comprised exclusively of SW tubes trapped in exfoliated regions, devoid of MWINT or other structures (see Fig. 7).

Sixteen zones encompassing multiple SW nanotubes were identified and localized through HRTEM analysis, which were subsequently

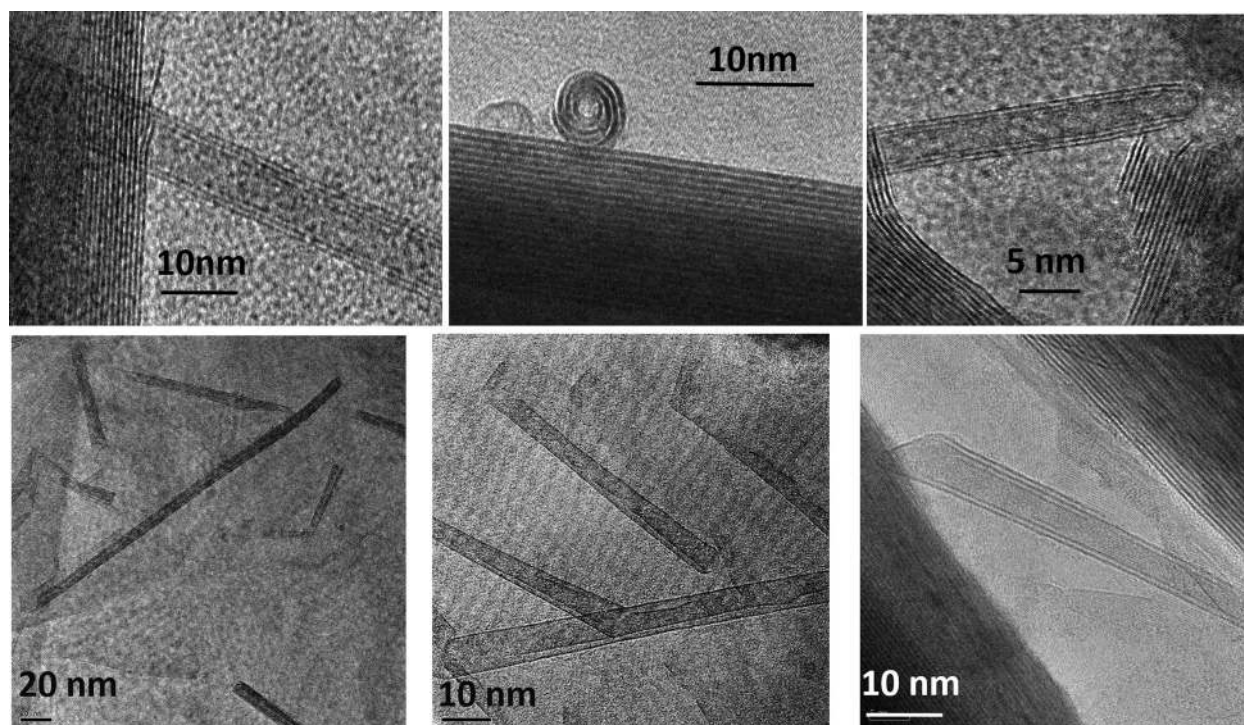


**FIG. 6.** Transmission electron microscopy images showing nanoscrolls and nanotubes of single to few layers and 3–7 nm diameter.

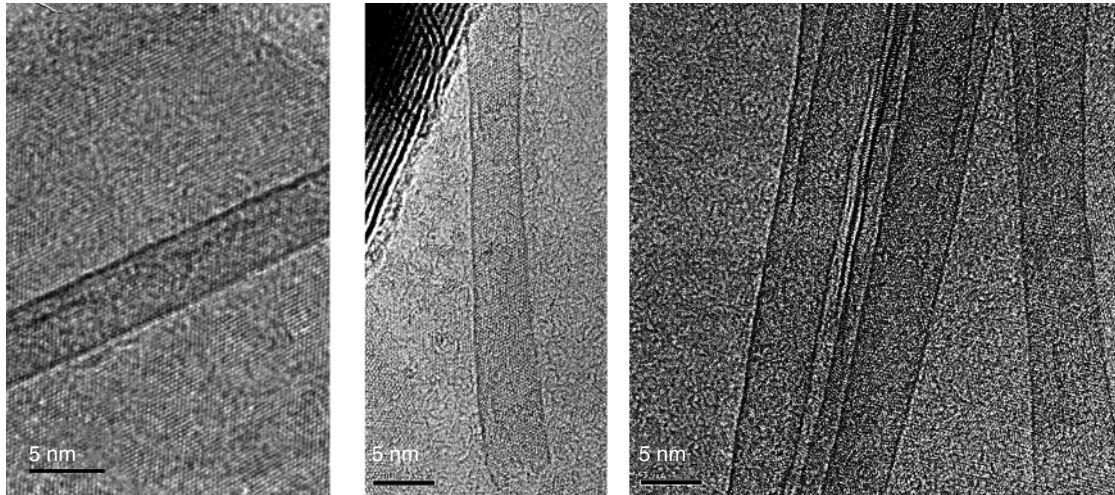


FIG. 7. Transmission electron microscopy images showing single layer  $WS_2$  nanotubes.

utilized for CL studies. A few (5–6) TEM images from each zone were acquired at different magnifications for pinning the exact location of SWINTs during SEM-CL measurements (see an example in Fig. 8).

### 3. CL measurements

The CL emission spectra, originated from native multiwall nanotubes, exfoliated (fluky) regions devoid of any SW tubes and regions with abundant entrapped SWINT, were collected using the SEM-CL. First, the regions containing SWINT (a few adjacent pixels on the mapping image) were located by SEM imaging through the preceding correlative TEM studies. Afterward, simultaneous SEM and CL imaging was performed to locate the luminescent regions. Panchromatic CL images were acquired using a PMT (photomultiplier tube). Then, CL spectra were collected either at specific points or by mapping a small area. The accelerating voltage was set to 20 kV (for the hyper spectral map) or 25 kV (for the point spectrum), with acquisition time of 30 s per pixel while using a 150 line/mm diffraction grating centred at 600 nm (2.06 eV). The spectra was collected at

–140 °C to improve the signal to noise ratio. Figure 9 displays the CL spectra of the (a)  $WS_2$  flakes (furls), (b) MW- and (c) SW-nanotubes, where the sharp peaks correspond to the direct bandgap of these nanostructures.

We have probed multiple locations (16 zones) with SW nanotubes and the representative result is shown here.

The excitonic effects play an important role in the luminescence behavior. Thus, the sharp peaks at 625 and 661 nm in the CL spectra of the different  $WS_2$  nanostructures [flakes (furls), MWINT, and SWINT] could be associated with the A exciton, while the broad peaks at higher energies (~513, 525, 530 nm) can be most likely assigned to the B exciton [see Fig. 9(a)–9(c)], both arose from direct gap transitions. A broad peak at the lower energy region (750–850 nm) could relate to the luminescence from the indirect bandgap or defect states in the nanotubes.<sup>43</sup>

The direct bandgap transitions (sharp peaks) for both flaky (furls) regions [Fig. 9(a)] and MWINT [Fig. 9(b)] devoid of single layered tubes were observed at 661 nm (1.87 eV). The regions comprising SW nanotubes alone produce the peak, related to the direct bandgap

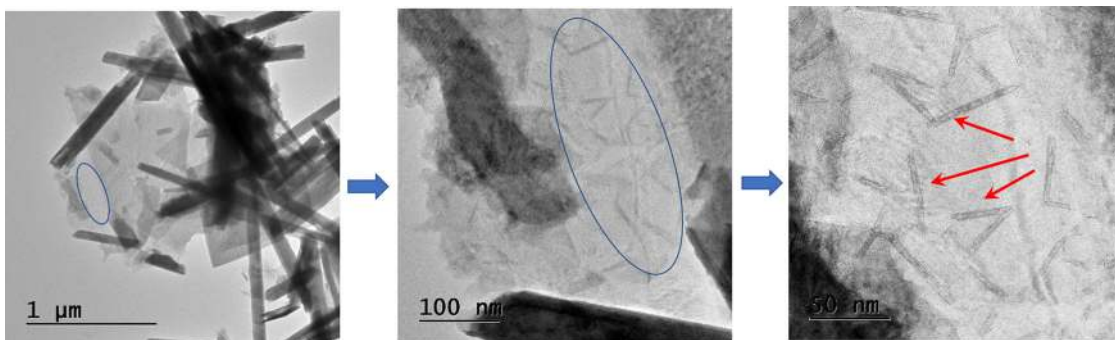
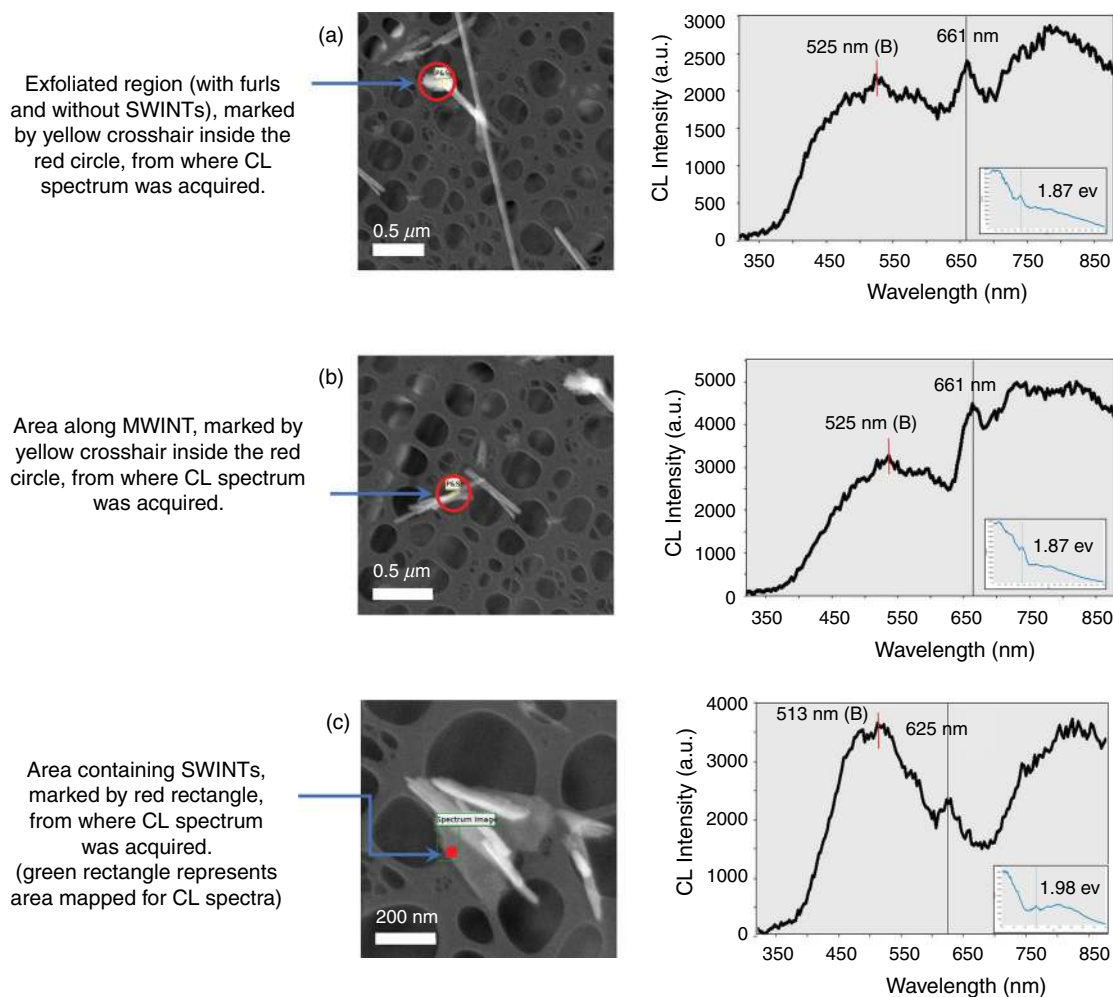


FIG. 8. Transmission electron microscopy images showing the procedure for fixing a location of a zone with daughter SW nanotubes at different magnifications gradually panning in. Blue circles and red arrows point on SW nanotubes.





**FIG. 9.** SEM images and CL spectrum acquired from (a) exfoliated zone (furls) devoid of any SWINTs, (b) MWINT and (c) a region containing SWINTs. (a) SEM image showing the exfoliated zone (marked by yellow crosshair in red circle) from where the CL spectrum was acquired; the CL spectrum reveals a sharp peak at 661 nm. (b) SEM image showing a MWINT along with the spot (yellow crosshair in red circle) from where the CL spectrum was acquired. The spectrum [right picture of panel (b)] shows a sharp peak at 661 nm. (c) SEM image of the region containing SWINT where the green rectangle represents the total area mapped for the CL study. Red rectangle represents a specific region containing SWINT (location of SWINTs was previously fixed through correlative TEM) from where the CL spectrum was acquired. The spectrum exhibits a sharp peak at 625 nm, exhibiting a blue shift of 36 nm (0.11 eV) compared to the CL spectra acquired from MWINTs and exfoliated zone devoid of SWINTs. The inset of each CL spectrum shows the corresponding CL intensity plotted against the energy. The peaks for the inset spectrum are observed at 1.87 eV for both (a) furls and (b) MWINT; the peak at 1.98 eV is obtained for (c) zone with the presence of SWINTs. The broad B excitonic peak initially observed in UV-visible spectrum at 517 nm is apparent in the CL spectra of furls, MWINT, and SWINT centered at (a) 525 nm (b) 530 nm, and (c) 513 nm, respectively.

transition, at 625 nm (bandgap of 1.98 eV) and exhibit a considerable blue shift ( $\sim 36$  nm or 0.11 eV) compared to MWINT.

The broad peak assigned to the B exciton, was observed at 525 and 530 nm (2.36 and 2.34 eV) on the CL spectra acquired from the exfoliated zone (with furls and without SWINTs) and multiwall nanotube, respectively, while the region containing SWINTs has B exciton peak at 513 nm (2.42 eV). This result is in agreement with the B exciton energy of mixed powder as deduced from the UV-visible (extinction) spectrum [517 nm (2.4 eV)], presented in Fig. 5. In analogy with the direct bandgap, associated with A exciton, the B exciton peak of SWINTs exhibits slight but distinct blue shift compared to MWINTs and exfoliated zones. The blue shift of the A and B excitonic peaks has

been previously observed for  $\text{WS}_2$  (and  $\text{WSe}_2$ ) flakes<sup>4</sup> and  $\text{WS}_2$  fullerene-like nanoparticles,<sup>13</sup> with a decrease the flake/wall thickness from 5 to 1 layer.

This blue shift of the SWINTs is a straight manifestation of the quantum confinement in the  $c$ -axis (perpendicular to the layers) due to decreasing number of layers,<sup>13</sup> and, hence, stemmed from a relatively large exciton radius (exceeding the layer thickness of  $\sim 3$  Å) in this direction for the SW tubes. Noticeably, the shift (0.11 eV) between MW and SW  $\text{WS}_2$  nanotubes is smaller than that observed previously in planar  $\text{WS}_2$  sheets ( $\sim 0.8$  eV)<sup>3</sup> by decreasing their thickness from bulk to monolayer. Moreover, a few layers of sheets are blue shifted compared to bulk.<sup>3,4</sup> Oppositely, the bandgap energies of both

MWINTs and SWINTs exhibit red shift compared to the bulk material gap (2.01–2.05 eV), which is in good agreement with previous studies and originates from the strain induced in the bent triple (S-W-S) layer of WS<sub>2</sub>.<sup>19,20</sup> Indeed, the deformations, curvature, and discommensuration between adjacent layers in onion-like and tubular NPs induce a red shift of the direct gap energy for multilayer INTs<sup>30</sup> and IFs<sup>13</sup> compared to 2H-WS<sub>2</sub>. Moreover, the red shift was found to be larger for MWINTs with smaller diameters<sup>19</sup> and for IFs containing more inner layers with smaller diameters,<sup>13</sup> which is opposite to the observed trend in CNTs with atomically thick layers,<sup>44</sup> and non-layered NPs.<sup>45–47</sup> This observation was confirmed by theoretical calculations exhibiting a sustainable increase in strain energy for the bent layers with a decrease in diameter.<sup>22,26</sup>

The SWINTs in this study have smaller diameters (3–7 nm) than MWINTs with 60–80 nm external and 20–30 nm internal diameters. Therefore, the spectral red shift for SWINTs, related to the strain in the lattice, is expected to be larger than that for the multiwall nanotubes. However, a lone layer of SWINT vs 20–30 layers in MWINTs also induces a strong quantum size effect in the z-direction, which usually is accompanied by a blue shift. Thus, the competitive upshot of strain and quantum confinement results in smaller value of the red shift for SWINTs than that of MWINTs vs bulk gap, or in a blue shift of SW vs MW, as demonstrated in the current study.

The comparative representation of the direct band gaps for the studied nanotubes and data available in the literature is depicted in Fig. 10(a). The WS<sub>2</sub> nanostructures included are: multiwall and single wall nanotubes of two different diameters, double wall nanotube, furl layers, plane monolayer sheet and bulk. Accordingly, smaller diameter MWINTs ( $D_1$  vs  $D_2$ ) as well as SWINTs ( $d_1$  vs  $d_2$ ) have smaller gaps (larger strain and, therefore, larger red shift compared to the bulk material), while the gap of a single wall tube is blue shifted (large confinement effect) compared to that of MWINTs and a double wall nanotube with the same external diameter. A qualitative strain-energy dependence on nanostructures' size and number of layers, as reported in the literature<sup>19,20,22,26,30</sup> and present study, is presented in Fig. 10(b).

Similar results were obtained by comparing the optical absorption spectra obtained for MWINTs, planar nanoflake structures exfoliated from MWINTs and bulk WS<sub>2</sub>.<sup>48</sup> It was found that the A- and B-exciton peaks of few layered planar flakes exhibit a blue shift compared to that of both nanotubes and bulk, while MW nanotubes were red shifted relative to the bulk (2H-WS<sub>2</sub> platelets). The blue shift of nanoflakes was ascribed to two factors: release of strain by straightening after exfoliation from furred MWINTs and quantum confinement along the *c*-axis due to the small number of layers.

Interestingly, Frey *et al.*<sup>13</sup> found that below a critical number of layers ( $n < 5$ ) in onion-like IFs 20–200nm in diameter, the excitons (both A and B) are blue shifted compared to the bulk. Above this number of layers, the excitonic transitions are red shifted as compared to 2H-WS<sub>2</sub> bulk platelets. Thus, it can be inferred that for IF nanoparticles with low ( $< 5$ ) numbers of layers, the quantum confining effect of carriers is predominant between the two effects, possibly due to the relatively large IFs' diameter and, therefore, smaller strain.

It should be noted that the exfoliated region without any SW tubes did not show any blue shift compared to the MWINTs. This was unexpected as the tubular conformation introduces lattice strain within the bent layers, which diminishes for flaky structures, and should result in a blue shift for flakes compared to NTs. This might be ascribed to the fact that these flaky nanostructures are multilayer and, being originated through exfoliation of the MWINTs during plasma treatment, are partially bent, resulting in a bandgap similar to that of MWINTs.

### C. Theoretical calculations

*Ab initio* calculations for the determination of the structural, electronic, and optical properties of single wall and multiwalled zigzag and armchair WS<sub>2</sub> nanotubes, of planar single layers, multilayers, and bulk WS<sub>2</sub>, have been carried out using the DFT and TDDFT methods. The technical details of the calculations are presented in the [supplementary material](#).

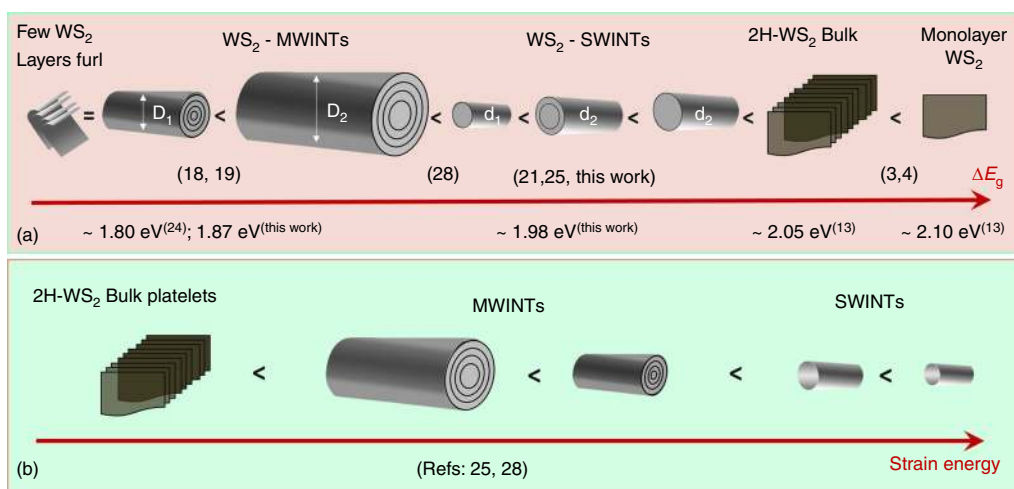


**FIG. 10.** Comparative representation of the (a) WS<sub>2</sub> band gaps for bulk material, monolayer sheet, few layers furl, nanotubes of different diameters, and amount of layers, analyzed here with CL spectra and in the literature using other techniques. (b) Comparative representation of strain energy in the WS<sub>2</sub> bulk material and nanotubes of different diameters and amount of layers as reported in the literature and present study. ( $d/D$  - diameter of SW/MWINT, respectively).

Specifically, we have investigated single wall WS<sub>2</sub> nanotubes of different chiralities and diameters: armchair (8,8), (10,10), (12,12), (14,14), (16,16) nanotubes and zigzag (16,0), (20,0), (24,0), (28,0), (32,0) nanotubes. We also studied the representative double-walled (10,10)@(16,16), (16,0)@(28,0), and (20,0)@(32,0) nanotubes. In addition, we have studied the planar monolayer, bilayer, trilayer, and the bulk WS<sub>2</sub>. A detailed description and explanation of the fundamental structural aspects of these systems, as given by the DFT computations, can be found in previous works by some of the present authors.<sup>49,50</sup>

The calculated electronic gaps between occupied and unoccupied states of armchair and zigzag single wall WS<sub>2</sub> nanotubes are shown as a function of the nanotube diameter in Fig. 11(a); and Tables II and III of the [supplementary material](#) give the numerical values of diameters and gaps for armchair and zigzag nanotubes, respectively. Those tables also include data for double wall nanotubes. The range of diameters studied is between 1.5 and 3.5 nm. The behaviour of the gap is similar for both types (armchair and zigzag) of nanotubes: the electronic bandgap decreases steeply as the nanotube diameter is reduced. In the double wall nanotubes (see Tables II and III of the [supplementary material](#)), the electronic gap is in between the gaps of the two isolated single wall tubes forming the double wall tube. Our calculated gaps are in good agreement with those reported by S. Piskunov *et al.*,<sup>51</sup> and the trend with nanotube diameter is the same.

We now turn to compare the calculations with the experimental results for the CL presented above. Previous studies on WS<sub>2</sub> and analogous MoS<sub>2</sub> nanotubes<sup>22,23,51</sup> have found that their stabilities, as measured by the strain energy, follow the 1/D<sup>2</sup> behavior, where D is the external diameter of the nanotubes (diameter of the external S layer of the exterior S-W-S trilayer). Our results for the strain energy per atom, plotted in Fig. 11(b), reproduce the 1/D<sup>2</sup> behavior. On the other hand, those previous studies exhibited a near independence of the strain energy from the tube chirality, while our calculated strain energies show that the zigzag nanotubes are unambiguously more stable than the armchair nanotubes, as shown in Fig. 11(b). The difference in

strain energies between the armchair and zigzag nanotubes is tiny but distinct, while the strain energy of zigzag tubes is systematically smaller than that of armchair nanotubes for all studied diameters. Moreover, using the fitted curves, this difference was calculated, exhibiting a decrease from 62 to 7 meV as the nanotube diameter increases from 1.5 to 3.5 nm. Interestingly, the obtained result and previously reported direct gap nature (essential for CL) of zigzag tubes<sup>26</sup> suggest that preferential formation of nanotubes with zigzag chirality should be expected in the synthesis experiments. Accordingly, the experimental CL results have to be compared with the theoretical calculations done for zigzag nanotubes, in our opinion. In fact, in the analysis that we present next, the experimental CL is consistent with the theoretical results based on zigzag nanotubes, which can be taken as a confirmation of formation of the zigzag nanotubes in the experimental CL study.

The experimental gap from CL experiments is 1.87 eV for multi-wall tubes, and 1.98 eV for single wall tubes: there is a blue shift of 0.11 eV when going from multiwall to single wall. The calculations also predict a blue shift if we compare double wall and single wall tubes of the same (approximate) diameter. For instance (see Table III of the [supplementary material](#)), in the case of zigzag tubes, the gap of the double wall (16,0)@(28,0) tube is 1.82 eV, and the gap of the single wall (28,0) tube is 2.27 eV (blue shift = 0.45 eV); the gap of the double wall (20,0)@(32,0) is 1.99 eV, and that for the single wall (32,0) is 2.31 eV (blue shift = 0.32 eV). One can observe that the magnitude of the blue shift decreases as the tube diameter increases. In the case of armchair nanotubes (see Table II of the [supplementary material](#)), the gap of the double wall (10,10)@(16,16) nanotube is 1.99 eV, and the gap of the single wall (16,16) tube is 2.21 eV; so the blue shift is 0.22 eV.

However, one has to keep in mind that standard DFT does not provide an accurate description of excited electronic states, and consequently, the electronic gaps calculated by standard DFT do not provide an accurate account of the experimental excitation threshold. This

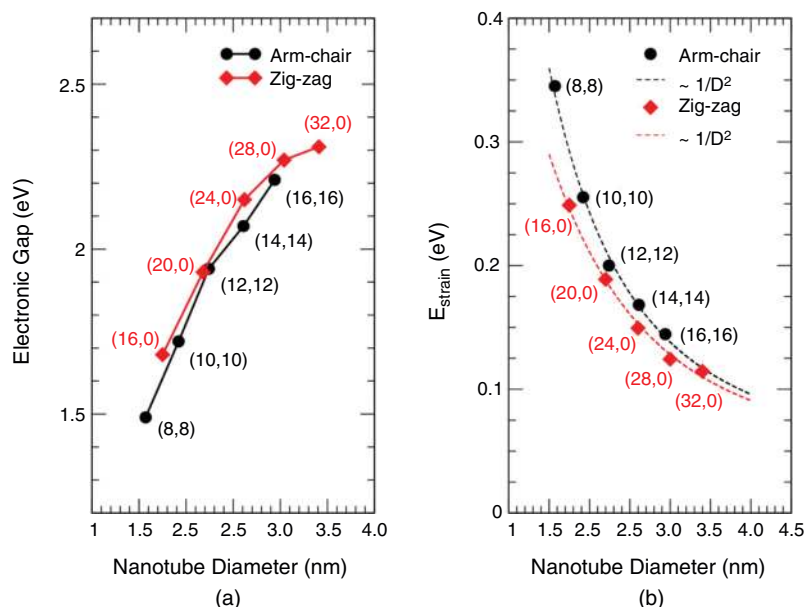


**FIG. 11.** (a) Electronic band gaps (in eV) between occupied and unoccupied electronic states and (b) strain energy (in eV) of the single wall armchair and zigzag WS<sub>2</sub> nanotubes as a function of the nanotube diameter (in nm). The strain energy was defined as the difference between the total energies per atom of the single wall nanotubes (with different diameters) and 2D periodic WS<sub>2</sub> planar monolayer (constant value).

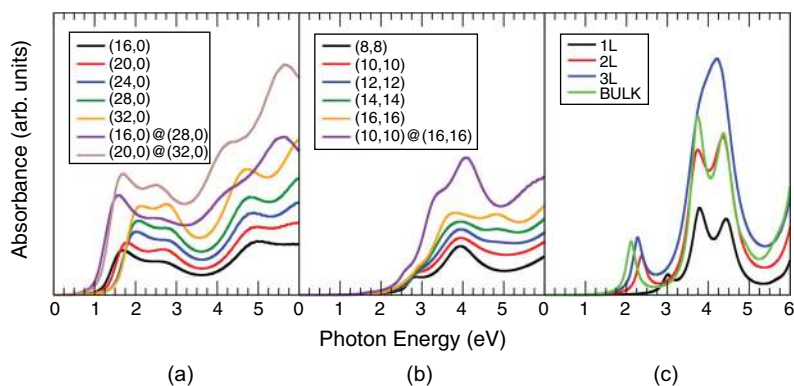


**FIG. 12.** Calculated absorbance as a function of photon energy (eV) for: (a) single and double wall zigzag nanotubes, (b) single and double wall armchair nanotubes, and (c) planar few-layers (with one, two, and three layers), and bulk. The absorbance spectra were calculated using Time-Dependent Density Functional Theory.

deficiency is overcome in part by TDDFT, which allows for a better description of the excited states and a more confident comparison with the experimental excitation spectrum. However, some many-body effects beyond TDDFT may still affect the electronic excitations<sup>52</sup> and are not included in the calculations. The calculated photoabsorption spectra obtained by TDDFT show peaks and the position of the first peak (the absorption threshold) can be identified with the experimental CL bandgap. By construction, those peaks have some width, and this sets limits to the precision with which the adsorption threshold can be estimated.

The calculated absorbance spectra of single wall and double wall nanotubes, planar few-layers and bulk are reported in Fig. 12. The zigzag single wall nanotubes show two peaks for energies below 3 eV. Those two peaks can be seen more clearly in the expanded Fig. 13(a), where the energy of the first peak (absorption threshold) is indicated for each curve in the legend of the figure. The energy of the absorption threshold of the single wall zigzag nanotubes is between 1.69 eV (16,0) and 2.14 eV (32,0), and increases with increasing nanotube diameter [see Fig. 13(b) and Table III of the supplementary material]. The absorption thresholds for the tubes with the larger diameters [(24,0), (28,0), (32,0)] are consistent with the gap measured in the CL experiments for single wall nanotubes: 1.98 eV. It is also noticeable that the average of the five calculated absorption thresholds is 1.94 eV. By comparing the threshold energies of double wall and single wall zigzag nanotubes, a clear blue shift is evident: the threshold energies of the single wall tubes are larger than

the threshold energies of the double wall tubes. The precise position of the second peak in the calculated absorption spectrum of zigzag nanotubes is more difficult to determine, because the peak is broad. The estimated averaged values from the spectra plotted in Fig. 13(a) for double wall and single wall nanotubes are 2.55 eV and 2.75 eV, respectively. These values show a blue shift from double wall to single wall tubes, which is consistent with the corresponding blue shift between multiwall and single wall tubes observed in the B exciton measured in the CL experiments. The B exciton features in the CL and UV-visible experiments are also broader than the A feature.

The spectra of armchair nanotubes in Fig. 12(b) also show two peaks. The second peak of the single wall armchair tubes is located at energies close to 4 eV and is very weakly dependent on tube diameter. The adsorption thresholds (first peak) are between 2.78 and 2.89 eV (see Table II of the supplementary material). This peak is barely visible in some tubes because it is masked by the strong and wide second peak. A blue shift from multiwall to single wall nanotubes is also evident in the absorbance threshold of armchair nanotubes. However, the adsorption thresholds of armchair nanotubes differ from the experimental CL gap, and this provides support to the expectation that the nanotubes formed in the experiment are likely zigzag tubes. Figure 12(c) shows the absorption spectra for planar few-layers with one, two, and three layers, as well as the spectrum of the bulk material. The calculated absorption thresholds are 3.01 eV (monolayer), 2.37 eV (bilayer), 2.27 eV (trilayer), and 2.12 eV (bulk), and the value for the

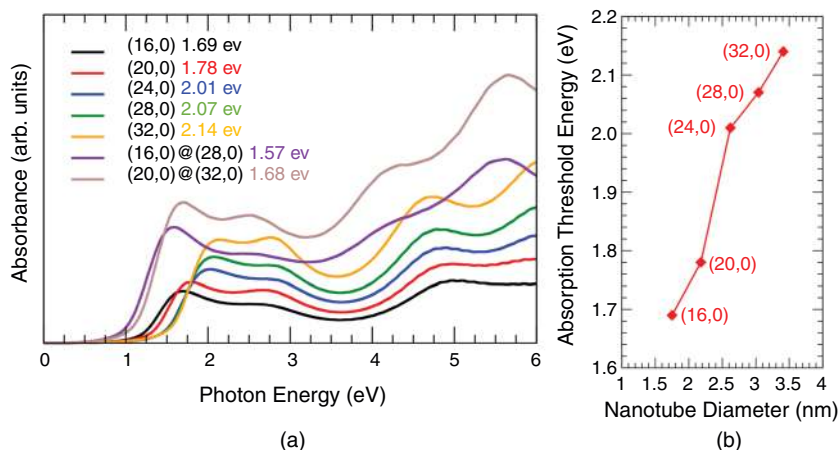


**FIG. 13.** (a) Calculated absorbance as a function of photon energy for single wall and double wall zigzag nanotubes. The threshold energies of different tubes are indicated in the legend. (b) Absorption threshold (in eV) plotted as a function of the nanotube diameter (in nm) for the single wall tubes.

bulk material is in excellent agreement with the previously measured bulk gap of 2.01–2.05 eV.<sup>19,20</sup> A blue shift of the single layer with respect to the few-layers is again noticed. The blue shift of the monolayer with respect to the bulk is 0.89 eV, in good agreement with the experimental blue shift of  $\sim 0.8$  eV.<sup>3</sup> Also consistent with experiment is the blue shift for the bilayer and trilayer with respect to the bulk.<sup>3,4</sup>

A final comparison can be made for the nanotubes vs bulk WS<sub>2</sub>. The results in Fig. 13 (see also Table III of the [supplementary material](#)) reveal a red shift in the adsorption thresholds of both double wall and SWINTs [except of (32,0) tube, in which case the absorption thresholds are nearly the same] compared to the bulk material, which is consistent with the behaviour of the current experimental band gaps. We should notice that the CL experiment was done at  $-140$  °C, while the absorption data were taken at RT ( $\sim 25$  °C) and the DFT and TDDFT are made for 0 K. Thus, the small differences between measured gaps and calculated absorption thresholds could be mainly ascribed to temperature variations.

#### IV. CONCLUSIONS

To summarize, this article presents an experimental measurement of CL of single and multiwall WS<sub>2</sub> nanotubes. It provides the first experimental evidence of quantum confinement in a single layer inorganic nanotube compared to MWINTs, through a considerable blue shift of 36 nm (110 meV) observed in the CL spectra. In addition, the bandgap energies of both MW- and SWINTs revealed red shift compared to the bulk material gap due to strain induced by the bent S-W-S triple layers of WS<sub>2</sub>. Actually, the changes in bandgap energy of INTs (as well as other furled layered nanostructures) vs bulk material reflect a competitive effect of the bending related strain and the quantum confinement. Both of these experimental observations (blue and red shifts) are in good agreement with the TDDFT based theoretical models presented here. Estimated band gaps for SWINTs by this model are red shifted compared to the bulk and blue shifted compared to the nanotubes modeled with two layers. Agreement of calculated values for gaps of zigzag (rather than for armchair) tubes with experiment, and estimated strain energies point at preferential formation of zigzag SWINTs in plasma reactor.

The protocol for producing single layer nanotubes by plasma treatment of MWINT has been modified to optimize the quality and yield of the former. This article also discusses a TEM correlated technique for the localization of SWINTs nanotubes on the TEM finder grids so as to investigate them further through CL studies by SEM-CL.

The ability to tune the electronic structure with morphology or number of layers may be exploited, for example, towards photoelectrochemical water splitting with WS<sub>2</sub> catalysts, devising FETs and photodetectors.

Future plans: To study CL vs number of layers, layers' chirality and size of nanotube, which have direct implications on their band structure. To calculate bandgap variations in SW, MW vs bulk. To check if indirect-to-direct band transition happens upon reduction of number of layers in the nanotubes.

#### SUPPLEMENTARY MATERIAL

The [supplementary material](#) contains information on the synthesis and characterization of single wall inorganic nanotubes (SWINTs). It entails the experimental setup for plasma treatment of multiwall nanotubes (MWINTs), SEM images of samples prepared under

different plasma treatment conditions and XRD analysis of the specimens phase before and after plasma exposure. It also delineates the technical details of Density Functional (DFT) and Time-Dependent Density Functional (TDDFT) calculations and provides a table for variation of estimated bandgap and absorption threshold as a function of tube diameter and layers.

#### AUTHORS' CONTRIBUTIONS

All authors contributed equally to this manuscript. All authors reviewed the final manuscript.

#### ACKNOWLEDGMENTS

The research of A.Z. was supported by a grant from the Israel Science Foundation (No. 330/16). The work of J.A.A. was supported by Junta de Castilla y León (Grant No. VA021G18) and the University of Valladolid (GIR Physics of Nanostructures). J.L.M. acknowledges financial support from Spanish MINECO (No. MAT2017-85089-C2-1-R, RYC-2015-17730), Comunidad de Madrid via Programa de Investigación Tecnológicas 2018 (No. FOTOART-CM S2018/NMT-4367), and the innovation program under grant agreements 785219 and 881603 (GrapheneCore2 and GrapheneCore3-Graphene-based disruptive technologies, respectively). The authors are grateful to Dr. Alex Idelevich from HIT, who synthesized multiwall WS<sub>2</sub> nanotubes. The authors thank Dr. A. Quade and A. Albrecht, of the Leibniz Institute for Plasma Science and Technology, who performed the XPS and XRD analysis, respectively.

#### DATA AVAILABILITY

The data that support the findings of this study are available within the article and its [supplementary material](#).

#### REFERENCES

- <sup>1</sup>K. F. Mak, C. Lee, J. Hone, J. Shan, and T. F. Heinz, *Phys. Rev. Lett.* **105**, 136805 (2010).
- <sup>2</sup>A. Splendiani, L. Sun, Y. Zhang, T. Li, J. Kim, C.-Y. Chim, G. Galli, and F. Wang, *Nano Lett.* **10**, 1271 (2010).
- <sup>3</sup>A. Kuc, N. Zibouche, and T. Heine, *Phys. Rev. B* **83**, 245213 (2011).
- <sup>4</sup>W. Zhao, Z. Ghorannevis, L. Chu, M. Toh, C. Kloc, P.-H. Tan, and G. Eda, *ACS Nano* **7**, 791 (2013).
- <sup>5</sup>B. Radisavljevic, A. Radenovic, J. Brivio, V. Giacometti, and A. Kis, *Nat. Nanotechnol.* **6**, 147 (2011).
- <sup>6</sup>D. Ovchinnikov, A. Allain, Y.-S. Huang, D. Dumcenco, and A. Kis, *ACS Nano* **8**, 8174 (2014).
- <sup>7</sup>B. Radisavljevic, M. B. Whitwick, and A. Kis, *ACS Nano* **5**, 9934 (2011).
- <sup>8</sup>B. Radisavljevic, M. B. Whitwick, and A. Kis, *Appl. Phys. Lett.* **101**, 043103 (2012).
- <sup>9</sup>A. Steinhoff, J.-H. Kim, F. Jahnke, M. Rösner, D.-S. Kim, C. Lee, G. H. Han, M. S. Jeong, T. O. Wehling, and C. Gies, *Nano Lett.* **15**, 6841 (2015).
- <sup>10</sup>C. Cong, J. Shang, Y. Wang, and T. Yu, *Adv. Opt. Mater.* **6**, 1700767 (2017).
- <sup>11</sup>C. Mai, A. Barrette, Y. Yu, Y. G. Semenov, K. W. Kim, L. Cao, and K. Gundogdu, *Nano Lett.* **14**, 202 (2014).
- <sup>12</sup>M. A. U. Absor, H. Kotaka, F. Ishii, and M. Saito, *Phys. Rev. B* **94**, 115131 (2016).
- <sup>13</sup>G. L. Frey, S. Elani, M. Homyonfer, Y. Feldman, and R. Tenne, *Phys. Rev. B* **57**, 6666 (1998).
- <sup>14</sup>Y. Feldman, G. L. Frey, M. Homyonfer, V. Lyakhovitskaya, L. Margulis, H. Cohen, G. Hodes, J. L. Hutchison, and R. Tenne, *J. Am. Chem. Soc.* **118**, 5362 (1996).
- <sup>15</sup>M. Hershinkel, L. A. Gheber, V. Voltera, J. L. Hutchison, L. Margulis, and R. Tenne, *J. Am. Chem. Soc.* **116**, 1914 (1994).

- <sup>16</sup>T. Köhler, Th. Frauenheim, Z. Hajnal, and G. Seifert, *Phys. Rev. B* **69**, 193403 (2004).
- <sup>17</sup>M. Coté, M. L. Cohen, and D. J. Chadi, *Phys. Rev. B* **58**, R4277 (1998).
- <sup>18</sup>G. Seifert, *AIP Conf. Proc.* **544**, 415 (2000).
- <sup>19</sup>M. Staiger, P. Rafailov, K. Gartsman, H. Telg, M. Krause, G. Radovsky, A. Zak, and C. Thomsen, *Phys. Rev. B* **86**, 165423 (2012).
- <sup>20</sup>L. Scheffer, R. Rosentzveig, A. Margolin, R. Popovitz-Biro, G. Seifert, S. R. Cohen, and R. Tenne, *Phys. Chem. Chem. Phys.* **4**, 2095 (2002).
- <sup>21</sup>B. Visic, R. Dominko, M. K. Gunde, N. Hauptman, S. D. Skapin, and M. Remskar, *Nanoscale Res. Lett.* **6**, 593 (2011).
- <sup>22</sup>G. Seifert, H. Terrones, M. Terrones, G. Jungnickel, and T. Frauenheim, *Phys. Rev. Lett.* **85**, 146 (2000).
- <sup>23</sup>G. Seifert, T. Köhler, and R. Tenne, *J. Phys. Chem. B* **106**, 2497 (2002).
- <sup>24</sup>B. L. Evans, in *Physics and Chemistry of Materials with Layered Structures*, edited by P. A. Lee (Reidel Dordrecht, 1979), Vol. 4, p. 1.
- <sup>25</sup>M. Bar-Sadan, M. Heidelmann, L. Houben, and R. Tenne, *Appl. Phys. A* **96**, 343 (2009).
- <sup>26</sup>N. Zibouche, A. Kuc, and T. Heine, *Eur. Phys. J. B* **85**, 49 (2012).
- <sup>27</sup>G. Seifert, H. Terrones, M. Terrones, G. Jungnickel, and T. Frauenheim, *Solid State Commun.* **114**, 245 (2000).
- <sup>28</sup>V. Jindal, S. Bhuyan, T. Deilmann, and S. Ghosh, *Phys. Rev. B* **97**, 045211 (2018).
- <sup>29</sup>C. Ballif, M. Regula, P. E. Schmid, M. Remskar, R. Sanjines, and F. Levy, *Appl. Phys. A* **62**, 543 (1996).
- <sup>30</sup>M. Ghorbani-Asl, N. Zibouche, M. Wahiduzzaman, A. F. Oliveira, A. Kuc, and T. Heine, *Sci. Rep.* **3**, 2961 (2013).
- <sup>31</sup>V. Brüser, R. Popovitz-Biro, A. Albu-Yaron, T. Lorenz, G. Seifert, R. Tenne, and A. Zak, *Inorganics* **2**, 177 (2014).
- <sup>32</sup>M. Kang, B. Kim, S. H. Ryu, S. W. Jung, J. Kim, L. Moreschini, C. Jozwiak, E. Rotenberg, A. Bostwick, and K. S. Kim, *Nano Lett.* **17**, 1610 (2017).
- <sup>33</sup>A. Raja, A. Chaves, J. Yu, G. Arefe, H. M. Hill, A. F. Rigosi, T. C. Berkelbach, P. Nagler, C. Schüller, T. Korn, C. Nuckolls, J. Hone, L. E. Brus, T. F. Heinz, D. R. Reichman, and A. Chernikov, *Nat. Commun.* **8**, 15251 (2017).
- <sup>34</sup>A. Zak, L. Sallacan-ecker, A. Margolin, M. Genut, and R. Tenne, *Nano* **04**, 91 (2009).
- <sup>35</sup>P. Chithaiah, S. Ghosh, A. Idelevich, L. Rovinsky, T. Livneh, and A. Zak, *ACS Nano* **14**, 3004 (2020).
- <sup>36</sup>C. Chen, A. Ogino, X. Wang, and M. Nagatsu, *Diam. Relat. Mater.* **20**, 153 (2011).
- <sup>37</sup>X. Mao, Y. Xu, Q. Xue, W. Wang, and D. Gao, *Nanoscale Res. Lett.* **8**, 430 (2013).
- <sup>38</sup>Y. Yomogida, Z. Liu, Y. Ichinose, and K. Yanagi, *ACS Omega* **3**, 8932 (2018).
- <sup>39</sup>L. Yadgarov, B. Visić, T. Abir, R. Tenne, A. Y. Polyakov, R. Levi, T. V. Dolgova, V. V. Zubyuk, A. A. Fedyanin, E. A. Goodilin, T. Ellenbogen, R. Tenne, and D. Oron, *Phys. Chem. Chem. Phys.* **20**, 20812 (2018).
- <sup>40</sup>S. S. Sinha, A. Zak, R. Rosentsveig, I. Pinkas, R. Tenne, and L. Yadgarov, *Small* **16**, 1904390 (2020).
- <sup>41</sup>V. Myroshnychenko, J. Nelayah, G. Adamo, N. Geuquet, J. Rodríguez-Fernandez, I. Pastoriza-Santos, K. F. MacDonald, L. Henrard, L. M. Liz-Marzan, N. I. Zheludev, M. Kociak, and F. J. G. de Abajo, *Nano Lett.* **12**, 4172 (2012).
- <sup>42</sup>T. Coenen, B. J. M. Brenny, E. J. Vesseur, and A. Polman, *MRS Bull.* **40**, 359 (2015).
- <sup>43</sup>D. Kazanov, M. Rakhlin, A. Poshakinskiy, and T. Shubina, *Nanomaterials* **10**, 373 (2020).
- <sup>44</sup>T. W. Odom, J.-L. Huang, P. Kim, and C. M. Lieber, *Nature* **391**, 62 (1998).
- <sup>45</sup>E. Oksenberg, A. Merdasa, L. Houben, I. Kaplan-Ashiri, A. Rothman, I. G. Scheblykin, E. L. Unger, and E. Joselevich, *Nat. Commun.* **11**, 489 (2020).
- <sup>46</sup>Y. Park, R. Yoo, S. R. Park, J. H. Lee, H. Jwang, H.-S. Lee, and W. Lee, *Sens. Actuators B: Chem.* **290**, 258 (2019).
- <sup>47</sup>M. El-Hagary, E. R. Shaaban, S. H. Moustafa, and G. M. A. Gad, *Solid State Sci.* **91**, 15 (2019).
- <sup>48</sup>C. L. Choi, J. Feng, Y. Li, J. Wu, A. Zak, R. Tenne, and H. Dai, *Nano Res.* **6**, 921 (2013).
- <sup>49</sup>A. Laikhtman, G. Makrinich, M. Sezen, M. M. Yildizhan, J. I. Martínez, D. Dinescu, M. Prodana, M. Enachescu, J. A. Alonso, and A. Zak, *J. Phys. Chem. C* **121**, 11747 (2017).
- <sup>50</sup>J. I. Martínez, A. Laikhtman, H. R. Moon, A. Zak, and J. A. Alonso, *Phys. Chem. Chem. Phys.* **20**, 12061 (2018).
- <sup>51</sup>S. Piskunov, O. Lisovski, Y. F. Zhukovskii, P. N. D'yachkov, R. A. Evarestov, S. Kenmoe, and E. Spohr, *ACS Omega* **4**, 1434 (2019).
- <sup>52</sup>J. I. Martínez, J. M. García-Lastra, M. J. López, and J. A. Alonso, *J. Chem. Phys.* **132**, 044314 (2010).